

This discussion paper is/has been under review for the journal Atmospheric Chemistry and Physics (ACP). Please refer to the corresponding final paper in ACP if available.

# Lidar and radar measurements of the melting layer in the frame of the Convective and Orographically-induced Precipitation Study: observations of dark and bright band phenomena

P. Di Girolamo<sup>1</sup>, D. Summa<sup>1</sup>, R. Bhawar<sup>1</sup>, T. Di Iorio<sup>2</sup>, E. G. Norton<sup>3</sup>, G. Peters<sup>4</sup>, and Y. Dufournet<sup>5</sup>

<sup>1</sup>Dipartimento di Ingegneria e Fisica dell'Ambiente, Università degli Studi della Basilicata, Potenza, Italy

<sup>2</sup>Dipartimento di Fisica, Università degli Studi di Roma "La Sapienza", Roma, Italy

<sup>3</sup>School of Earth, Atmospheric & Environmental Sciences, University of Manchester, Manchester, UK

<sup>4</sup>Meteorologisches Institut, Universität Hamburg, Hamburg, Germany

<sup>5</sup>Delft University of Technology, Delft, The Netherlands

30949

Received: 20 August 2011 – Accepted: 31 October 2011 – Published: 21 November 2011

Correspondence to: P. Di Girolamo (digirolamo@unibas.it)

Published by Copernicus Publications on behalf of the European Geosciences Union.

Discussion Paper

Discussion Paper

Discussion Paper

Discussion Paper

Discussion Paper

Discussion Paper

Discussion Paper

Discussion Paper

30950

**Abstract**

During the Convective and Orographically-induced Precipitation Study (COPS), lidar dark and bright bands were observed by the University of BASILicata Raman lidar system (*BASIL*) during several intensive (IOPs) and special (SOPs) observation periods (among others, 23 July, 15 August, and 17 August 2007). Lidar data were supported by measurements from the University of Hamburg cloud radar *MIRA 36* (36 GHz), the University of Hamburg dual-polarization micro rain radars (24.1 GHz) and the University of Manchester UHF wind profiler (1.29 GHz). Results from *BASIL* and the radars for 23 July 2007 are illustrated and discussed to support the comprehension of the microphysical and scattering processes responsible for the appearance of the lidar and radar dark and bright bands. Simulations of the lidar dark and bright band based on the application of concentric/eccentric sphere Lorentz-Mie codes and a melting layer model are also provided. Lidar and radar measurements and model results are also compared with measurements from a disdrometer on ground and a two-dimensional cloud (2DC) probe on-board the ATR42 SAFIRE.

**1 Introduction**

Changes in scattering properties of precipitating particles are found to take place during the snowflake-to-raindrop transition in the proximity of the freezing level. A maximum in radar reflectivity, known as the radar bright band, is observed in the microwave domain, while a minimum in lidar echoes appears at optical wavelengths, this phenomenon being referred as lidar dark band (Sassen and Chen, 1995).

The radar bright band has been known and studied for more than three decades and it is presently a well understood phenomenon (Battán, 1973; Meneghini and Liao, 2000). The radar bright band phenomenon is dominated by Rayleigh dielectric scattering effects. As snowflakes descend below the freezing level inside the melting layer, their radar reflectivity increases as a result of melting, because the dielectric constant

30951

of water exceeds that of ice by a factor of approximately 5 (Rogers and Yau, 1989). Lower in the melting layer, snowflakes collapse into raindrops; since rain drops fall faster than snowflakes, their volume concentration is reduced. This reduction in concentration is the primary cause for the decrease of reflectivity observed in the lower part of the melting layer. While the radar bright band is ubiquitous in the S and L band, only intermittent evidence is found in the K and W bands (Sassen et al., 2005), because of the dominance in these latter bands of non-Rayleigh scattering effects.

Unlike the radar bright band, the lidar dark band has been poorly investigated and, to date, no systematic and coordinated observations are available. Lidar observations of the lidar dark band have been reported by Sassen and Chen (1995), Demoz et al. (2000) and Roy and Bissonnette (2001). Model simulations of this phenomenon have been provided by several authors (Di Girolamo et al., 2003; Griaznov et al., 2004). The lidar dark band is believed to be the result of two conflicting microphysical processes: a) the structural collapse of severely melted snowflakes, leading to a decrease of lidar backscattering due to the reduced particles size and concentration and b) the completion of the melting process, leading to an increase of lidar backscattering associated with spherical particle backscattering mechanisms coming into prominence (Sassen and Chen, 1995). The radar bright band peak occurs in the melting region, just above (approx. 200 m) the lidar dark-band minimum, this position being close to where radar Doppler velocity reaches its plateau. A lidar bright band has been also occasionally reported (Sassen et al., 2005; Di Girolamo et al., 2003), associated with additional scattering processes involving melting hydrometeors.

A comprehensive study of the dark and bright band phenomena has been published by Sassen et al. (2005), where the authors report measurements performed by a single-wavelength (523 nm) backscatter lidar system and a three-wavelength Doppler radar (0.32-, 0.86-, and 10.6 cm). Unfortunately, in the paper by Sassen et al. (2005) lidar and radar depolarization data, which would have provided further information on the state of the melting particles, were not available from the instruments involved. Instead, lidar and radar depolarization measurements of the melting particles were

30952

Discussion Paper | Discussion Paper | Discussion Paper | Discussion Paper | Discussion Paper | Discussion Paper | Discussion Paper | Discussion Paper | Discussion Paper | Discussion Paper

Poorly investigated usually strongly under? suggest reviewing sentence

523 nm

Forget Sassen et al 2007

How does concentration change?  
a) is incomplete suppression of backscatter off of rear face of droplet surrounding collapsed snowflake  
See Fig 5 Sassen et al 2005

performed during COPS by *BASIL* and *MIRA 36*, respectively, and are reported in the present paper together with multi-wavelength lidar measurements of the particle backscattering.

## 2 Lidar and radar systems

5 The measurements illustrated in this paper were performed in the framework of COPS – Convective and Orographically-induced Precipitation Study – held in Southern Germany and Eastern France in the period 1 June–31 August 2007 (Wulfmeyer et al., 2008; Richard et al., 2009). COPS was conceived with the primary goal of advancing the quality of forecasts of orographically induced convective precipitation by four-  
10 dimensional observations and modeling of its life cycle (Kottmeier et al., 2008; Kalthoff et al., 2009; Wulfmeyer et al., 2011). *BASIL* was deployed throughout the duration of COPS in Supersite R (Achern, Rhine Valley, Lat: 48.64° N, Long: 8.06° E, Elev.: 140 m). The system operated between 25 May and 30 August 2007 and collected more than 500 h of measurements, distributed over 58 measurement days. Quicklooks of the  
15 data are visible on the COPS Website (<http://www.cops2007.de/>), under Operational Products, while the data can be downloaded from the World Data Center for Climate (<http://cera-www.dkrz.de/WDCC/ui/BrowseExperiments.jsp?proj=COPS>) ~~of~~ requested ~~to~~ the authors.

of

The major feature of *BASIL* is ~~represented by~~ its capability to perform high-resolution and accurate measurements of atmospheric temperature and water vapour, both in  
20 daytime and night-time, based on the application of the rotational and vibrational Raman lidar techniques in the UV (Di Girolamo et al., 2004, 2006, 2009a; Bhawar et al., 2011). Besides temperature and water vapour, *BASIL* measures particle backscatter at 355, 532 and 1064 nm, particle extinction coefficient at 355 and 532 nm and particle  
25 depolarization at 355 and 532 nm (Maestri et al., 2010; Griaznov et al., 2007; Di Girolamo et al., 1996, 2009b). *BASIL* is not protected from precipitation and therefore cannot be operated when rain reaches the ground. However, a careful and conser-

30953

vative operation of the system till shortly before ~~the~~ precipitation reaches the ground allowed us to capture several precipitation episodes involving melting hydrometeors.

During COPS, lidar data were supported by measurements from the University of Hamburg cloud radar *MIRA 36* (36 GHz, 0.83 cm, Ka-band), the University of Hamburg  
5 dual-polarization micro rain radars (24.1 GHz, 1.24 cm, K-band) and the University of Manchester UHF wind profiler (1.29 GHz, 23.24 cm, UHF band) (Norton et al., 2006). The three zenith-pointing radars represent a unique combination of microwave sensors. Atmospheric probing at the shortest wavelengths (0.83 and 1.24 cm) is sensitive to  
10 cloud droplets and ice crystals. In contrast to the K- and Ka-band radars, the UHF radar (23.24 cm) cannot generally observe ~~the~~ particles suspended in a cloud, but rather observes the larger precipitation particles, whose returned radar signals can be treated relatively simply with Rayleigh scattering theory. It should be pointed out that none of the previously reported measurements of the lidar and radar dark/bright bands could rely on multi-wavelength lidar backscatter, extinction and depolarization data, as well as on multi-wavelength radar reflectivity, depolarization and Doppler velocity data.

REFERENCES →



Why should this be pointed out?

Ancillary information on the state of the atmosphere was provided by radiosondes, launched every three hours during each measurement session, as well as by a sodar and a microwave radiometer. Additional information on precipitating hydrometeors are obtained from a disdrometer, located on ground in the proximity of the lidar and the  
20 radars, and a two-dimensional cloud (2DC) probe (Appendix A), on-board the scientifically equipped aircraft ATR42 from Service des Avions Français Instrumentés pour la Recherche en Environnement (SAFIRE), whose participation to COPS was supported by the European Commission under the European Fleet for Airborne Research (EU-FAR) program of the 7th Framework Program. This large "ensemble" of instruments makes the collected dataset unique for the purpose of studying precipitating hydrometeors in the melting layer.

- 1.) This is a massive run-on sentence.
- 2.) Move to Acknowledgements

you guys keep saying this??  
Send to previous page, too.  
FWIW, the Sassen et al. study in a 2005 had many of these data streams, as part of NASA CRYSTAL-FACE.  
He just didn't make use of them because they didn't want what he wanted accomplished in that paper.

30954



velocities is also found in the melting layer (Fig. 6), as a result of the melting process leading to smaller particles with a more regular shape and smaller impact area. Values of Doppler vertical velocity are not exceeding  $2\text{--}3\text{ ms}^{-1}$  above and in the upper part of the melting layer, while larger values ( $> 4\text{ ms}^{-1}$ ) appear in the lower portion of the melting layer.

Figures should be (a) - (e) to avoid confusion like

Figure 7 illustrates the lidar and radar data expressed in terms of averaged vertical profiles, together with ancillary information from the radiosonde data. Specifically, the left panel shows the vertical profile of temperature as measured by the radiosonde launched at 14:06 UTC, revealing the height of the freezing level at  $\sim 3.35\text{ km a.g.l.}$  The second panel from left shows the vertical profiles of radar reflectivity at 36 GHz, 24.1 GHz and 1.29 GHz, revealing the presence of the radar bright band (reflectivity maximum) at  $2.9\text{--}3.0\text{ km a.g.l.}$ , i.e.  $350\text{--}450\text{ m}$  below the freezing level at a temperature of  $3.4\text{--}4.4\text{ }^\circ\text{C}$ . Radar profiles in this and the other panels are based on 12 min data averaging over the time interval 14:23–14:35 UTC. The third panel from left shows the vertical profiles of the backscattering coefficient at 355, 532 and 1064 nm, highlighting the presence of a lidar dark band (backscattering minimum) at approximately  $2.9\text{ km}$ , i.e.  $450\text{ m}$  below the freezing level at a temperature of  $4.4\text{ }^\circ\text{C}$ , while a lidar bright band is found approximately  $100\text{--}200\text{ m}$  further down at  $2.7\text{--}2.8\text{ km a.g.l.}$  Dark band signatures appear also in the lidar measurements of particle extinction at 355 and 532 nm (not shown here). Lidar profiles in this and the other panels are based on 15 min data averaging over the time interval 14:20–14:35 UTC. The fourth panel from left shows the vertical profile of vertical velocity as measured at 36 GHz, 24.1 GHz and 1.29 GHz. Values at 36 GHz and 1.29 GHz are  $2\text{--}2.5\text{ ms}^{-1}$  high in the melting layer and  $3.5\text{--}4\text{ ms}^{-1}$  in the lower portion of the melting layer. Values measured by the rain radar at 24.1 GHz show slightly larger values high in the melting layer (as large as  $3.5\text{ ms}^{-1}$ ) and in the lower portion of the melting layer (as large as  $4\text{--}4.5\text{ ms}^{-1}$ ), probably as a result of the larger sensitivity of the 24.1 GHz band to larger and consequently faster particles. Lidar (at 355 nm) and radar (at 36 GHz) depolarization are shown in the fifth panel from left of Fig. 7.

30957

Enhanced radar reflectivity and depolarization and an abrupt change in Doppler-derived particle velocities are found in the melting layer (radar bright band). Radar depolarization is increased (up to approximately 60%) due to the presence of wetted, asymmetric ice shapes. In contrast to this, lidar depolarization at 355 nm shows values of  $25\text{--}30\%$  high in the melting layer and values of  $5\text{--}10\%$  at the heights of the lidar dark and bright bands. These unexpectedly low values of lidar depolarization may imply that precipitating particles are almost spherical or have a more regular shape.

The fall speed of the precipitating hydrometeors can be inferred from the particle backscatter data by tracing the particle streams. Figure 8 shows again the particle backscatter ratio at 1064 nm, considering a different colour scale with respect to the one used in Fig. 1 in order to highlight hydrometeors. Precipitation appears as distinct streams: some of these are not reaching the surface as a result of particle evaporation/sublimation or exit from the field-of-view of the lidar system. Similar tilted structures are also present in the radar reflectivity plots in Figs. 2–4. The slope of the precipitation streams in the time-height map allows to roughly quantify the fall speed of the precipitating hydrometeors, based on the assumption no horizontal advection of the precipitating particles. Fall speed estimates are in the range  $4.5\text{--}9\text{ ms}^{-1}$ . These values are in agreement with the vertical velocities measured by the radar at 36 GHz and 1.29 GHz (Fig. 7).

### 3.2 Model simulations

The main purpose of this section is to provide a possible model simulation of the observed lidar backscatter measurements. Computations of the scattering properties of the melting hydrometers and simulations of the lidar dark and bright bands are performed based on the application of concentric/eccentric sphere Lorentz-Mie codes and a melting layer model. The concentric/eccentric sphere codes consider a melting hydrometeor consisting of an ice core surrounded by a water shell (Yokoyama and Tanaka, 1984). The concentric/eccentric water/ice sphere model may apply to conditions in the initial melting process Sassen et al. (2005), when the melting snowflake

30958

Discussion Paper | Discussion Paper | Discussion Paper | Discussion Paper | Discussion Paper | Discussion Paper | Discussion Paper | Discussion Paper | Discussion Paper | Discussion Paper

NO see discussion outside

actually consists of myriad water coatings and irregular drop beads. Figure 9 illustrates the variability of the volume backscattering coefficient at 350 nm,  $\beta_{355}$ , as a function of the melting ratio, i.e. the core/shell radius ratio,  $r_c/r_s$ , as simulated through the application of the concentric sphere code. Simulations in the optical domain (350 nm) for hydrometeors with a radius of 1.5 mm imply particle size parameter values (that is, the ratio of the particle circumference over the sounding wavelength) in excess of 25 000 (Di Girolamo et al., 2003). This imposes long computation times and a careful check for numerical stability.

The figure reveals the presence of an abrupt increase of  $\beta_{355}$  for melting ratio values  $r_c/r_s$  of 0.6–0.8, which is to be attributed to the major role played in the backscatter process of severely melted hydrometeors by rays with large impact factors. It is to be pointed out that coalescence and breakup are completely ignored in this model. A melting model (Yokoyama and Tanaka, 1984) was considered to compute the variability of  $r_c/r_s$  as a function of the range below the 0°C isotherm. Ranges below the freezing level obtained from this model are reported on the right scale of Fig. 9, with results for two different melting particle radii (1.5 and 3.0 mm). From these results we realize that the backscattering enhancement found for  $r_c/r_s$  values of 0.6–0.8 takes place approximately 250–340 m below the freezing level for hydrometeors of 1.5 mm and 400–580 m below the freezing level for hydrometeors of 3.0 mm, in agreement with the lidar measurements in Fig. 7.

The severely melted ice core can move to the top or bottom of the drop (Pruppacher and Beard, 1970; Rasmussen et al., 1984). Specifically, the core can float to the top of the water drop if it has entrapped air bubbles or can flutter around inside the drop due to drag-induced internal circulations (Pruppacher and Beard, 1970).

So, we also considered a Mie code for large particles with off-centre inclusions, with the ice core at the top or bottom of the water shell (Fig. 10). The considered code is capable of dealing with size parameter values up to ~1000.

Figure 11 illustrates the variability of  $\beta_{355}$  as a function of the melting ratio. Results are obtained with a size parameter  $x = 600$ , which corresponds to a hydrometeor radius

30959

of 35  $\mu\text{m}$ . A strong enhancement in backscatter coefficient is observed for a melting ratio of 0.55 when the ice core is at top of water shell and for a melting ratio of 0.8 when the ice core is at bottom of water shell; these results being in general agreement with those obtained with the concentric sphere code. Considering the results in terms of ranges below the freezing level obtained from the above mentioned melting model, we realize that the backscattering maxima found for  $r_c/r_s$  values of 0.55 and 0.8 take place 250–350 m below the freezing level for hydrometeors with a radius of 1.5 mm and 400–600 m below the freezing level for hydrometeors with a radius of 3.0 mm, these results being once again in general agreement with the lidar measurements in Fig. 7.

In a simplified schematic representation (Fig. 12), the lidar dark band can be interpreted as arising from the collapse of partially melted snowflakes, leading to a decrease of lidar backscattering as a result of the reduced particle size and concentration (few hundred meters below the freezing level), while the lidar bright band can be interpreted as arising from the progression of the melting process, leading to a sudden increase of lidar backscattering when the melting ratio is in the range 0.55–0.8, taking place further down (up to 600 m) in the melting layer. In reality of course, both concentric and eccentric sphere models are simplified representations, as the melting snowflakes are non-spherical mixes of ice, water and air, which cannot be modelled exactly.

### 3.3 2DC probe, rain radar and disdrometer measurements

Additional information on precipitating hydrometeors were provided by the 2DC probe and additional in situ sensors on-board the ATR42 SAFIRE (EUFAR initiative – OSMOC project). Figure 13 shows the time series of atmospheric temperature and relative humidity (upper panel), liquid water content (LWC, mid panel) and aircraft altitude (lower panel). This figure shows the aircraft descent path throughout the melting layer (red ellipse), with the freezing level being located around 3.35 km a.g.l.

We need to point out that the aircraft measurements were carried out approximately half an hour after the lidar measurements shown in Fig. 7 (no lidar measurements were possible after 14:35 UTC because of rain reaching the telescope) and that the footprint

30960

Melting

Melting

not right word... density??

Again, it's about precipitation then other matter, which your data agree with

of the aircraft is located at a distance of approximately 10–15 km from the lidar station. However, Figs. 2 and 3 reveal a very limited variability of the radar reflectivity profiles at 1.29 and 36 GHz in the two hour period following the end of the lidar measurements (14:30–16:30 UTC), indicating a lack of small-scale meteorological variability during this period. Consequently, the time and space lag between the aircraft and the lidar measurements only minorly affect the comparison between these measurements.

Figure 14 represents a magnification of Fig. 13 for the time interval (15:04–15:10 UTC) when the melting processes occurred, only for the parameters atmospheric temperature and aircraft altitude.

Figure 15 illustrates the two-dimensional images of the melting hydrometeors being probed by the 2DC probe mounted below the aircraft wings. We focused our attention on the final portion of the flight when the aircraft is descending through the melting layer (identified by the red ellipse in Fig. 13). This figure reveals the progressive melting of the snowflakes and the reduction of particle size, which is followed by an increase in size of the completely melted snowflakes (rain drops) associated with the collision-coalescence process. Based on a visual approach, five distinct time intervals can be identified, characterized by different precipitating particle types. Specifically, the time interval labelled as 1 (15:05:52–15:06:07, blue shadowed in the figure) identifies rimed aggregates, while time interval 2 (15:06:09–15:06:19, light blue shadowed in the figure) identifies mixed rain drops with few rimed aggregates. Time intervals 3–5 (interval 3, 15:06:19–15:06:38, green shadowed in the figure; interval 4, 15:06:42–15:08:31, red shadowed in the figure; interval 5, 15:08:33–15:11:02, yellow shadowed in the figure) identify rain drops with progressively increasing size as a result of the collision-coalescence process. These results are compatible with the model representation we have considered to simulate the scattering properties of the melting hydrometers and with the lidar depolarization measurements illustrated in the previous sections (characterized by low values in the melting region).

Figure 16 illustrates the melting hydrometeor size distribution as obtained from the time series of the two-dimensional images for the five distinct intervals. Specifically,

30961

How is your model any different than Sassen's?

Fig. 16a shows the particle size distribution for the rimed aggregates in the time interval 1 (15:05:52–15:06:07), with a total particle number concentration of  $0.49464 \text{ cm}^{-3}$ ; Fig. 16b shows the particle size distribution for the mixed rain drops and rimed aggregates in the time interval 2 (15:06:09–15:06:19), with a total particle number concentration of  $0.52066 \text{ cm}^{-3}$ . Figure 16c–e illustrates the particle size distribution for rain drops, with total particle number concentration being  $0.08389 \text{ cm}^{-3}$ ,  $0.18161 \text{ cm}^{-3}$  and  $0.09981 \text{ cm}^{-3}$  in the time interval 3, 4 and 5, respectively. A Marshall and Palmer size distribution was used to fit the data points in Fig. 16a–e. The Marshall and Palmer size distribution can be expressed as:

$n(D) = n_0 \exp(-\Lambda D)$  (1)

with the mean diameter  $D_0$  being equal to  $1/\Lambda$  (Pruppacher and Klett, 1997). As particle concentration in Fig. 16a–e is expressed in semi-log scale, for fitting purposes Eq. (1) can be reformulated as:

$\log n(D) = \log n_0 - \Lambda D$  (2)

Values of  $\Lambda$ , and consequently of  $D_0$ , for the different panels in Fig. 16 can be obtained by linear regression. To avoid overloading of the figures, the fitting curve is shown only in Fig. 16d. Values of  $D_0$  obtained from the fitting procedure are found to be 348, 305, 278, 421 and  $654 \mu\text{m}$  for the time intervals 1, 2, 3, 4 and 5, respectively, these results once again revealing that melting hydrometers progressively decrease in size during the melting process till they become raindrops (intervals 1 through 3); afterwards, they progressively increase in size, most probably as a result of the collision-coalescence process (intervals 3 through 5).

Figure 17 illustrates the precipitating particle size spectrum at 2 km a.g.l. as obtained from the rain radar at 24.1 GHz. The particle size spectrum in Fig. 17 is in good agreement with measurements performed by the 2DC probe. Also the data points in Fig. 17 have been least-squared fitted through the Marshall and Palmer size distribution function in Eq. (1), leading to a mean diameter of  $190 \mu\text{m}$ .

30962

Conceptually, this all makes sense. though it's nice to see this in real numbers





images have been fitted by a Marshall and Palmer function, leading to estimates of the melting hydrometeor diameter in the range 300–650  $\mu\text{m}$ , which are in agreement with analogous measurements from the rain radar and a disdrometer on ground.

As a future continuation of this study, we plan to extend the present analysis to all available case studies observed during COPS. Additionally, we plan to apply an inversion algorithm to retrieve precipitating particle size and microphysical parameters from the multi-wavelength lidar data of particle backscattering, extinction and depolarization, based on the use of a Mie scattering code and a retrieval scheme employing Tikhonov's inversion with regularization. More experimental data for a comprehensive understanding of melting layer phenomena are expected to be obtained from scanning dual-polarization lidar measurements, which were not available during COPS but are planned to be implemented in the future, as in fact inhomogeneous melting drops tend to orientate, so that a lidar elevation angle dependence of return signals may be present.

## Appendix A

The two-dimensional cloud (2DC) probe is mounted below the aircraft wings on-board the scientifically equipped ATR42 from Service des Avions Français Instrumentés pour la Recherche en Environnement. It provides two-dimensional images of the atmospheric particles, with a maximum detectable particle size of 2 mm. Measurements can be used to retrieve cloud and precipitating particle size distribution. An additional collocated sensor (Gerber PMV100) provides time series measurements of the aircraft altitude, atmospheric temperature and LWC. The 2DC probe is composed of two different branches: a linear array of 30 photodiodes (25  $\mu\text{m}$  each, with a total length of 800  $\mu\text{m}$ ) is located at the tip of one branch, while a diode laser illuminating the array of photodiodes is located at the tip of the opposite branch. The array is oriented perpendicular to the airflow, so that any time a particle passes in between the tips of the two branches, a certain number of photodiodes are shadowed, producing a line of black

30965

points. By sampling at an high rate of 10 Hz, the sequence of lines produces a two-dimensional image of the particles passing through the branches' tips. The particles images in the Fig. 15 are the representation of this time series of shadowed lines.

*Acknowledgements.* This work was supported by the European Commission under the European Fleet for Airborne Research program of the 7th Framework Program (Projects H<sub>2</sub>O Lidar and OSMOC). We also wish to thank the International Science Steering Committee of the Convective and Orographically-induced Precipitation Study for financial supporting this activity. We wish to thank the University of Kiel for the provision of the disdrometer data. The participation of T. Di Iorio to this work was supported through the project PRIN 2007L8Y4NB funded by the Italian Ministry for University and Research, MIUR.

## References

- Battan, L. J.: Radar Observations of the Atmosphere, University of Chicago Press, Chicago, USA, 279 pp., 1973.
- Bhawar, R., Di Girolamo, P., Summa, D., Flamant, C., Althausen, D., Behrendt, A., Kiemle, C., Bosser, P., Cacciani, M., Champollion, C., Di Iorio, T., Engelmann, R., Herold, C., Pal, S., Wirth, M., and Wulfmeyer, V.: The water vapour intercomparison effort in the framework of the convective and orographically-induced precipitation study: airborne-to-ground-based and airborne-to-airborne lidar systems, *Q. J. Roy. Meteor. Soc.*, 137, 325–348, doi:10.1002/qj.697, 2011.
- Demoz, B. B., Starr, D., Whiteman, D., Evans, K., Hlavka, D., and Peravali, R.: Raman LIDAR detection of cloud base, *Geophys. Res. Lett.*, 27(13), 1899–1902, 2000.
- Di Girolamo, P., Pappalardo, G., Berardi, V., Cuomo, V., Spinelli, N., and Velotta, R.: Lidar observations of the stratospheric aerosol layer over Southern Italy in the period 1991–1995, *J. Geophys. Res.*, 101, 18765–18773, 1996.
- Di Girolamo, P., Ambrico, P. F., Amodeo, A., Boselli, A., Pappalardo, G., and Spinelli, N.: Aerosol observations by lidar in the Nocturnal Boundary Layer, *Appl. Optics*, 38(21), 4585–4595, 1999.
- Di Girolamo, P., Demoz, B. B., and Whiteman, D. N.: Model simulations of melting hydrometeors: a new lidar bright band from melting frozen drops, *Geophys. Res. Lett.*, 30(12), 1626, doi:10.1029/2002GL016825, 2003.

30966

- Di Girolamo, P., Marchese, R., Whiteman, D. N., and Demoz, B. B.: Rotational Raman lidar measurements of atmospheric temperature in the UV, *Geophys. Res. Lett.*, 31, L01106, doi:10.1029/2003GL018342, 2004.
- Di Girolamo, P., Behrendt, A., and Wulfmeyer, V.: Pure rotational Raman lidar measurements of atmospheric temperature and extinction from space: performance simulations, *Appl. Optics*, 45, 2474–2494, 2006.
- Di Girolamo, P., Summa, D., and Ferretti, R.: Rotational Raman lidar measurements for the characterization of stratospheretroposphere exchange mechanisms, *J. Atmos. Ocean. Tech.*, 26, 1742–1762, 2009a.
- Di Girolamo, P., Summa, D., Lin, R.-F., Maestri, T., Rizzi, R., and Masiello, G.: UV Raman lidar measurements of relative humidity for the characterization of cirrus cloud microphysical properties, *Atmos. Chem. Phys.*, 9, 8799–8811, doi:10.5194/acp-9-8799-2009, 2009b.
- Griaznov, V., Veselovskii, I., Di Girolamo, P., Demoz, B., and Whiteman, D. N.: Numerical simulation of light backscattering by spheres with off-center inclusion. Application for Lidar case, *Appl. Optics*, 43, 5512–5522, 2004.
- Griaznov, V., Veselovskii, I., Di Girolamo, P., Korenskii, M., and Summa, D.: Spatial distribution of doubly scattered polarized laser radiation in the focal plane of a lidar receiver, *Appl. Optics*, 46, 6821–6830, 2007.
- Joss, J. and Waldvogel, A.: Precipitation measurement and hydrology, in: *Radar in Meteorology*, edited by: Atlas, D., Am. Meteorol. Soc., Boston, USA, 577–597, 1990.
- Kalthoff, N., Adler, B., Barthlott, C., Corsmeier, U., Mobbs, S., Crewell, S., Trummer, K., Kottmeier, C., Wieser, A., Smith, V., and Di Girolamo, P.: The impact of convergence zones on the initiation of deep convection: a case study from COPS, *Atmos. Res.*, 93, 680–694, 2009.
- Kottmeier, C., Kalthoff, N., Barthlott, C., Corsmeier, U., Van Baelen, J., Behrendt, A., Behrendt, R., Blyth, A., Coulter, R., Crewell, S., Di Girolamo, P., Dorninger, M., Flamant, C., Foken, T., Hagen, M., Hauck, C., Höller, H., Konow, H., Kunz, M., Mahlke, H., Mobbs, S., Richard, E., Steinacker, R., Weckwerth, T., Wieser, A., and Wulfmeyer, V.: Mechanisms initiating deep convection over complex terrain during COPS, *Meteorol. Z.*, 17, 931–948, 2008.
- Maestri, T., Di Girolamo, P., Summa, D., and Rizzi, R.: Synergistic use of a ground based RAMAN Lidar and the NAST-I Airborne Spectrometer in clear and cloudy sky conditions – EAQUATE, Italy 2004, *Atmos. Res.*, 97, 157–169, 2010.
- Meneghini, R. and Liao, L.: Effective dielectric constants of mixed-phase hydrometeors, *J. Atmos. Ocean. Tech.*, 17, 628–640, 2000.

30967

- Norton, E. G., Vaughan, G., Methven, J., Coe, H., Brooks, B., Gallagher, M., and Longley, I.: Boundary layer structure and decoupling from synoptic scale flow during NAMBLEX, *Atmos. Chem. Phys.*, 6, 433–445, doi:10.5194/acp-6-433-2006, 2006.
- Pruppacher, H. and Beard, K. V.: A wind tunnel investigation of the internal circulation and shape of water drops falling at terminal velocity in air, *Q. J. Roy. Meteorol. Soc.*, 96, 247–256, 1970.
- Pruppacher, H. R. and Klett, J. D.: *Microphysics of clouds and precipitation*, Kluwer Academic Publishers, Dordrecht and Boston, 954 pp., 1997.
- Rasmussen, R. M., Levizzani, V., and Pruppacher, H. R.: A wind tunnel and theoretical study on the melting behavior of atmospheric ice particles. II: A theoretical study for frozen drops of radius < 500 μm, *J. Atmos. Sci.*, 41(3), 374–380, 1984.
- Richard, E., Flamant, C., Bouttier, F., Van Baelen, J., Champollion, C., Hagen, M., Cuesta, J., Bosser, P., Pigeon, G., Argence, S., Arnault, J., Brousseau, P., Seity, Y., Chaboureaud, J.-P., Limnaios, P., Masson, F., Pointin, Y., Di Girolamo, P., and Wulfmeyer, V.: La campagne COPS : initiation et cycle de vie de la convection en région montagneuse, *La Météorologie*, 64, 32–42, 2009.
- Rogers, R. R. and Yau, M. K.: *A Short Course in Cloud Physics*, 3. edn., International Series in Natural Philosophy, Butterworth and Heinemann, Oxford, 304 pp., 1989.
- Roy, G. and Bissonnette, L. R.: Strong dependence of rain-induced lidar depolarization on the illumination angle: experimental evidence and geometrical-optics interpretation, *Appl. Optics*, 40, 4770–4780, 2001.
- Sassen, K. and Chen, T.: The lidar dark band: an oddity of the radar bright band, *Geophys. Res. Lett.*, 22, 3505–3508, 1995.
- Sassen, K., Campbell, J. R., Zhu, J., Kollias, P., Shupe, M., and Williams, C.: Lidar and triple-wavelength Doppler radar measurements of the melting layer: a revised model for dark and bright band phenomena, *J. Appl. Meteorol.*, 44, 301–312, 2005.
- Stewart, R. E., Marwitz, J. D., Pace, J. C., and Carbone, R. E.: Characteristics through the melting layer of stratiform clouds, *J. Atmos. Sci.*, 41, 3227–3237, 1984.
- Yokoyama, T. and Tanaka, H.: Microphysical processes of melting snowflakes detected by two-wavelength radar. Part I. Principle of measurement based on model calculation, *J. Meteorol. Soc. Jpn.*, 62, 650–666, 1984.
- Wulfmeyer, V., Behrendt, A., Bauer, H. S., Kottmeier, C., Corsmeier, U., Adrian, G., Blyth, A.,

30968

- Craig, G., Schumann, U., Hagen, M., Crewell, S., Di Girolamo, P., Flamant, C., Miller, M., Montani, A., Mobbs, S., Richard, E., Rotach, M. W., Arpagaus, M., Russchenberg, H., Schlüssel, P., König, M., Gärtner, V., Steinacker, R., Dorninger, M., Turner, D. D., Weckwerth, T., Hense, A., and Simmer, C.: The convective and orographically-induced precipitation study: a research and development project of the World Weather Research Program for improving quantitative precipitation forecasting in low-mountain regions, *B. Am. Meteorol. Soc.*, 89, 1477–1486, 2008.
- Wulfmeyer, V., Behrendt, A., Kottmeier, C., Corsmeier, U., Barthlott, C., Craig, G. C., Hagen, M., Althausen, D., Aoshima, F., Arpagaus, M., Bauer, H. S., Bennett, L., Blyth, A., Brandau, C., Champollion, C., Crewell, S., Dick, G., Di Girolamo, P., Dorninger, M., Dufournet, Y., Eigenmann, R., Engelmann, R., Flamant, C., Foken, T., Gorgas, T., Grzeschik, M., Handwerker, J., Hauck, C., Höller, H., Junkermann, W., Kalthoff, N., Kiemle, C., Klink, S., König, M., Krauss, L., Long, C. N., Madonna, F., Mobbs, S., Neining, B., Pal, S., Peters, G., Pigeon, G., Richard, E., Rotach, M. W., Russchenberg, H., Schwitalla, T., Smith, V., Steinacker, R., Trentmann, J., Turner, D. D., van Baelen, J., Vogt, S., Volkert, H., Weckwerth, T., Wernli, H., Wieser, A., and Wirth, M.: The Convective and Orographically Induced Precipitation Study (COPS): the scientific strategy, the field phase, and first highlights, *Q. J. Roy. Meteorol. Soc.*, 137, 3–30, 10.1002/qj.752, 2011.

30969

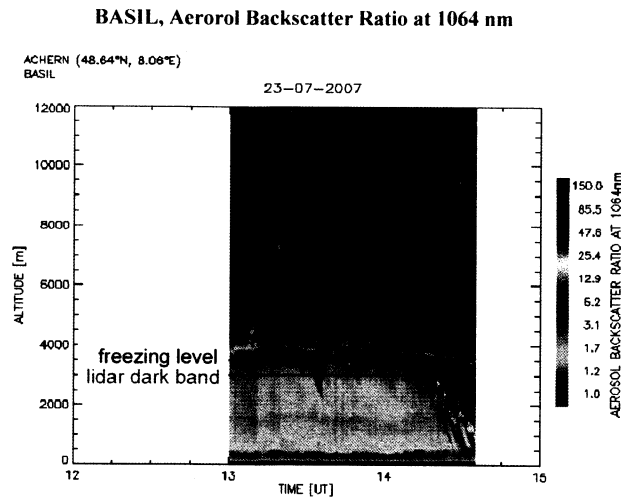


**Fig. 1.** Time evolution of the particle backscatter ratio at 1064 nm from 13:00 UTC to 14:35 UTC on 23 July 2007 as measured by the Raman Lidar system BASIL. Arrows highlight the location of the freezing level and the lidar dark band.

30970

University of Manchester Radio Wind Profiler, 1290 MHz UHF Doppler radar

23/07/2007

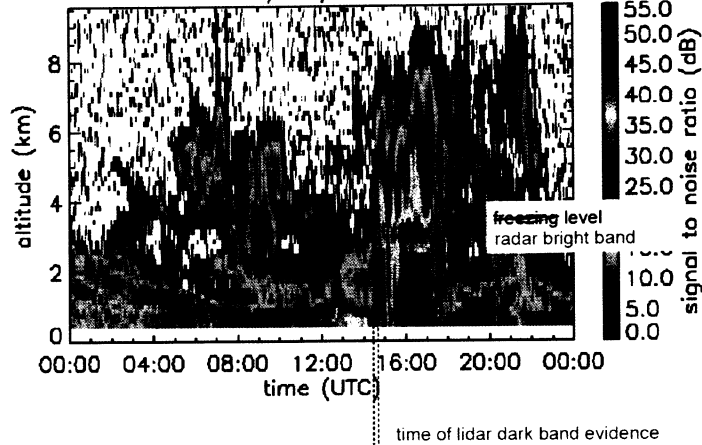


Fig. 2. Time evolution of radar reflectivity at 1.29 GHz from 00:00 UTC to 24:00 UTC on 23 July 2007 as measured by the clear air wind profiler. Arrows indicate the location of the freezing level and the radar bright band.

30971

### MIRA 36, Radar Reflectivity at 36 GHz

13.01 23.07.2007 - 16.00 23.07.2007 Achem

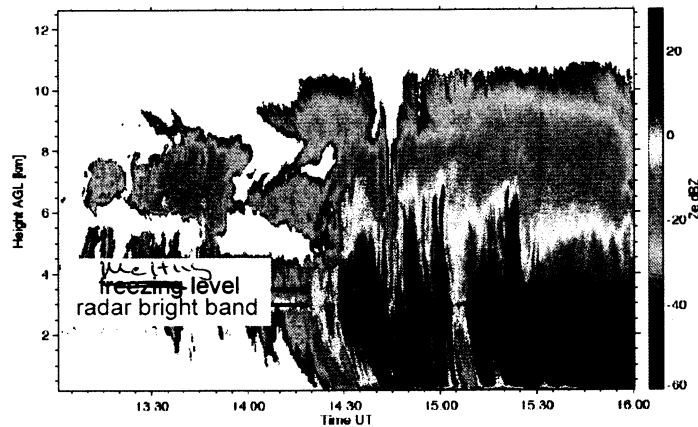
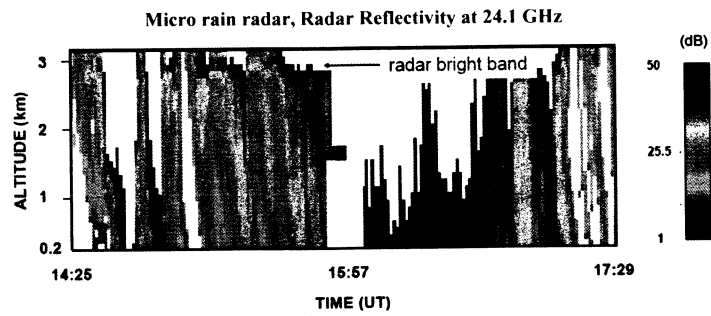


Fig. 3. Time evolution of radar reflectivity at 36 GHz from 13:00 UTC to 16:00 UTC on 23 July 2007 as measured by MIRA 36. Arrows indicate the location of the freezing level and the radar bright band.

30972



**Fig. 4.** Time evolution of radar reflectivity at 24.1 GHz from 14:25 UTC to 17:29 UTC on 23 July 2007 as measured by the micro rain radar. The red arrow indicates the location of the radar bright band.

30973

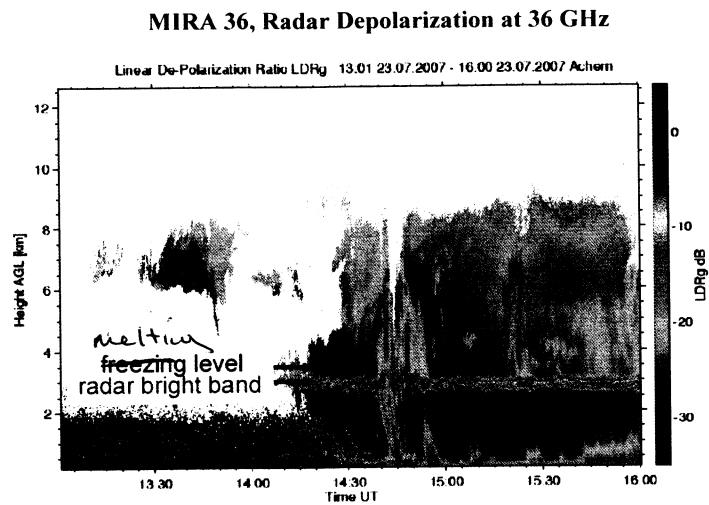


**Fig. 5.** Time evolution of the linear depolarization ratio at 36 GHz from 13:00 UTC to 16:00 UTC on 23 July 2007 as measured by MIRA 36.

30974

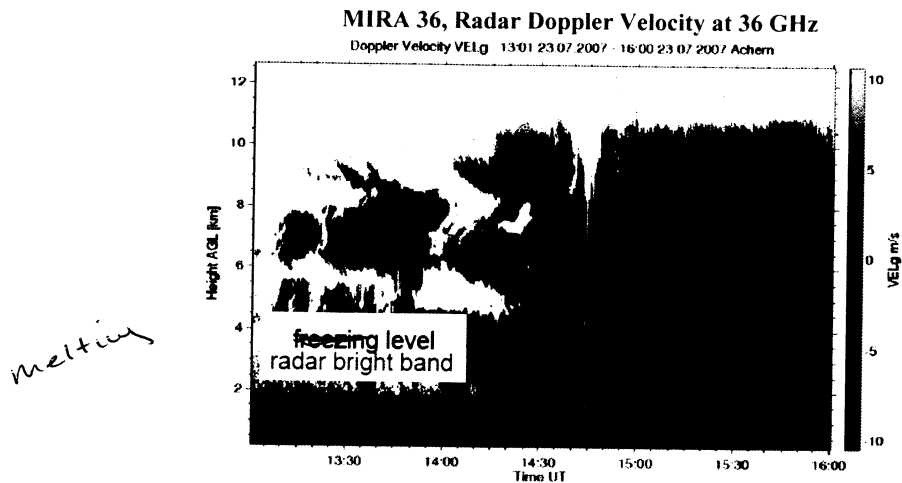


**Fig. 6.** Time evolution of hydrometeors vertical velocity from 13:00 UTC to 16:00 UTC on 23 July 2007 as measured by MIRA 36.

30975

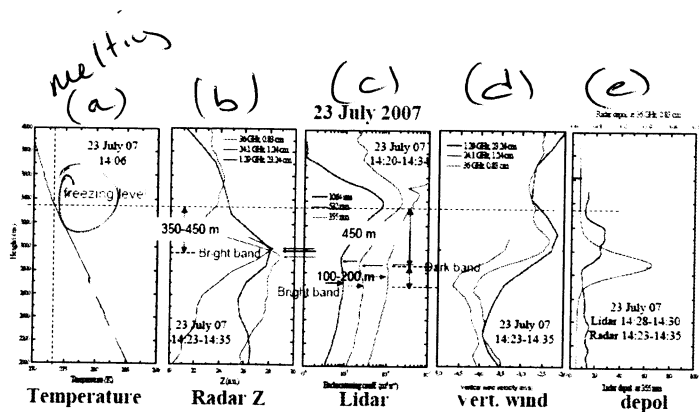


**Fig. 7.** Vertical profile of temperature as measured by the radiosonde launched at 14:06 UTC (left panel); vertical profile of radar reflectivity at 36 GHz, 24.1 GHz and 1.29 GHz (second panel from left); vertical profile of backscattering coefficient at 355, 532 and 1064 nm (third panel from left); vertical profile of vertical velocity measured at 36 GHz and 1.29 GHz (fourth panel from left); lidar (at 355 nm) and radar (at 36 GHz) depolarization (fifth panel from panel). In the second panel from the left the range of radar reflectivities has been compressed by subtracting 15 dBZ to the 1.29 GHz data.

30976

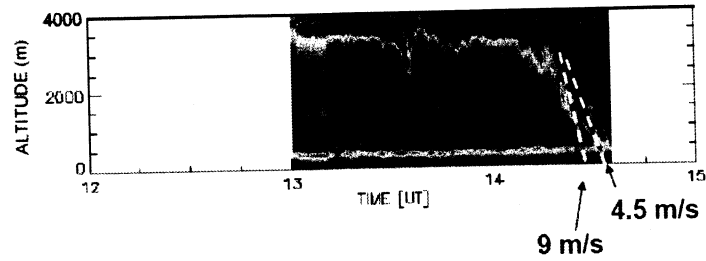


**Fig. 8.** Time evolution of the particle backscatter ratio at 1064 nm from 13:00 UTC to 14:35 UTC on 23 July 2007 as measured by the Raman Lidar system BASIL. In the figure the precipitating hydrometeors with different fall velocities appear as different particle streams with different slopes.

30977

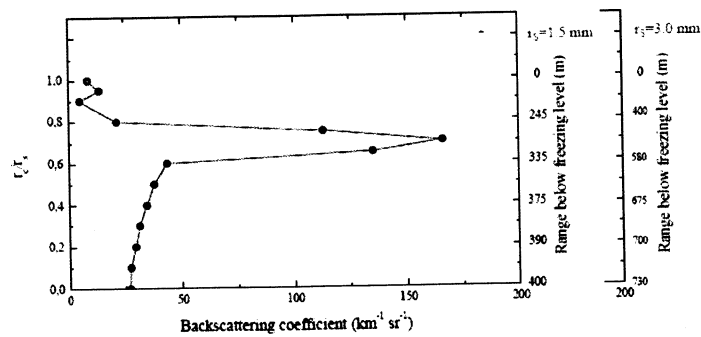


**Fig. 9.** Volume backscattering coefficient at 350 nm vs. melting ratio  $r_c/r_s$ .

30978

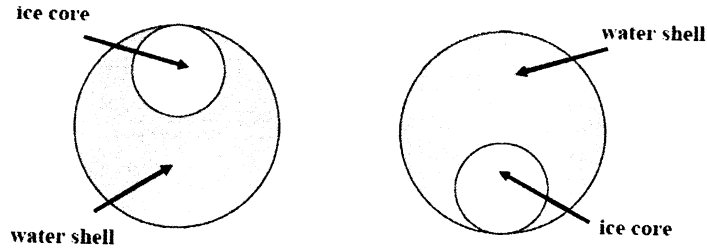


**Fig. 10.** Schematics of off-centre inclusion particles, with the ice core at the top or bottom of the water shell.

30979

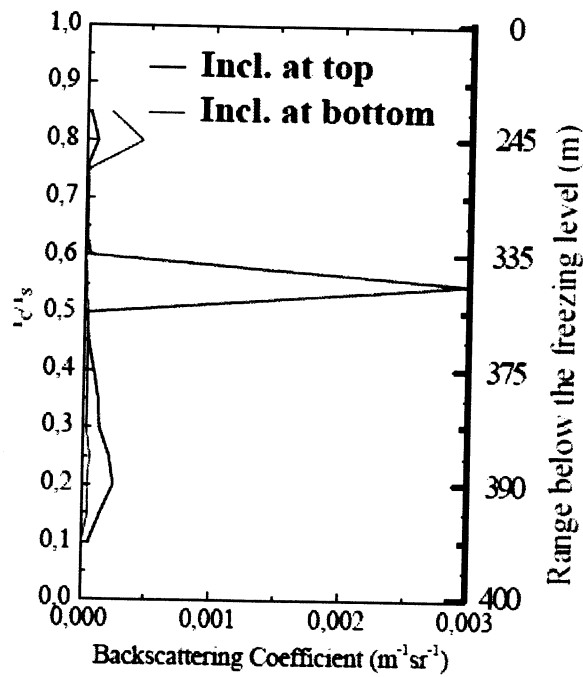


**Fig. 11.** Volume backscattering coefficient at 350 nm vs. melting ratio  $r_c/r_s$ , as simulated through the application of the eccentric sphere code.

30980



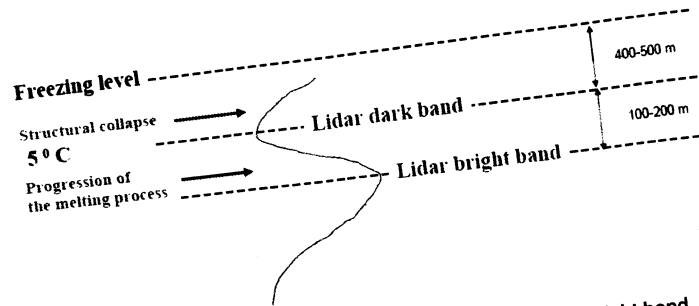


Fig. 12. Simplified schematic representation of the the lidar dark and bright band.

30981

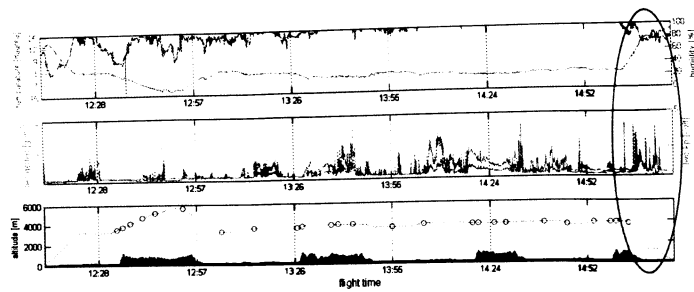
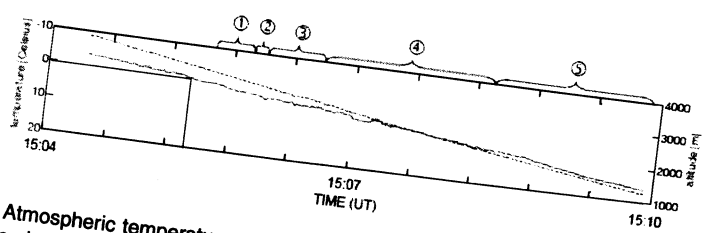


Fig. 13. Time series of atmospheric temperature and relative humidity (upper panel), liquid water content (mid panel) and aircraft altitude (lower panel).

30982



**Fig. 14.** Atmospheric temperature and aircraft altitude in the time interval 15:04–15:10 UTC. The figure also identifies five distinct time intervals characterized by different precipitating particle types and properties, which are discussed in detail in Figs. 15 and 16.

30983

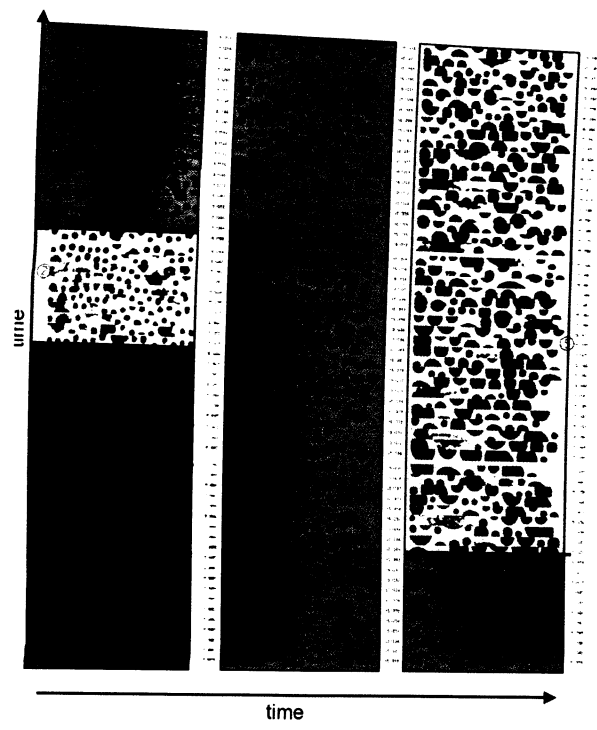


**Fig. 15.** Two-dimensional images of the melting hydrometeors probed by the 2DC. The five distinct time intervals 1–5 are characterized by different precipitating particle types and properties.

30984

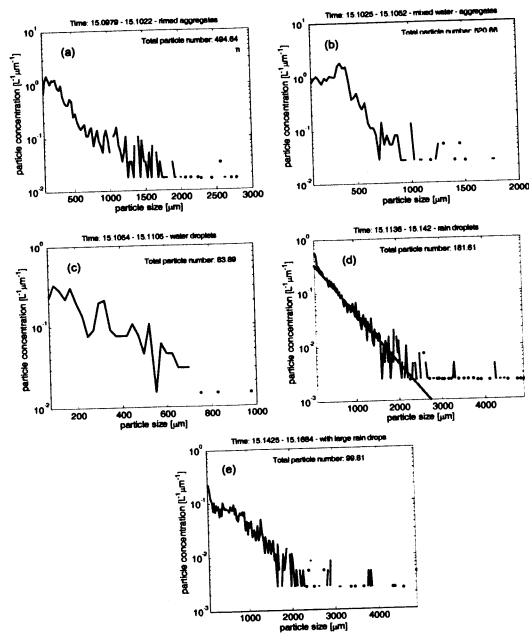


**Fig. 16.** Precipitating particle size distribution as obtained from the time series of the two-dimensional images. **(a):** time interval 1 (15:05:52–15:06:07), **(b):** time interval 2 (15:06:09–15:06:19), **(c):** time interval 3 (15:06:19–15:06:38), **(d):** interval 4 (15:06:42–15:08:31) and **(e):** interval 5 (15:08:33–15:11:02).

30985

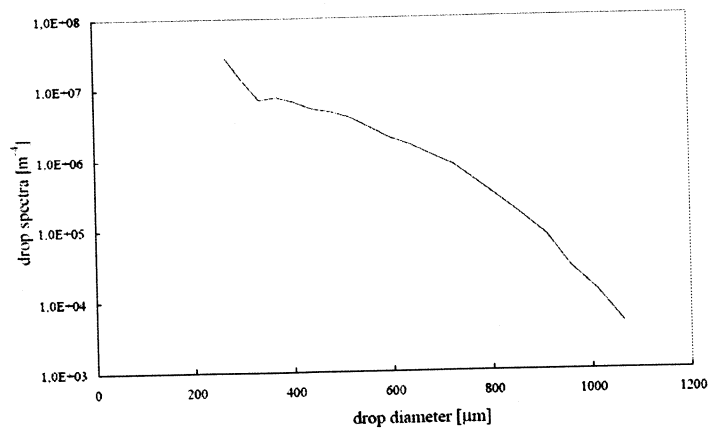


**Fig. 17.** Particle size spectrum as obtained from the rain radar.

30986

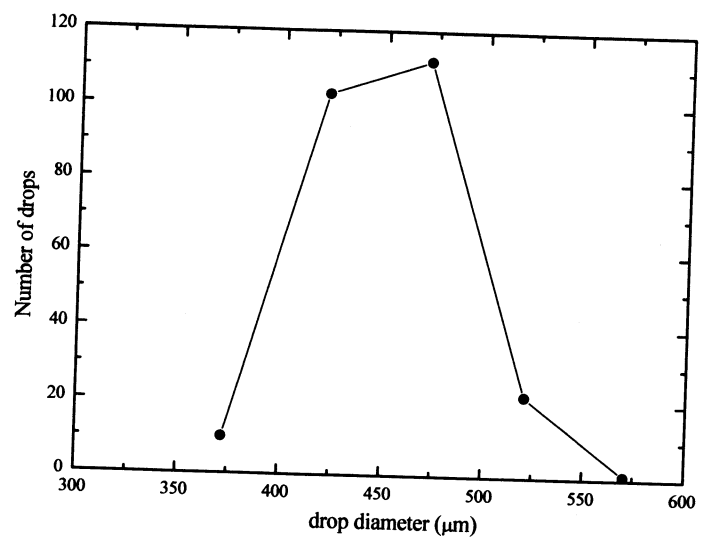


**Fig. 18.** Precipitating particle size distribution as obtained from the time series of the disdrometer measurements at ground level in Supersite *R*.